Monthly Notices of the ROYAL ASTRONOMICAL SOCIETY

MNRAS **518,** 3667–3674 (2023) https://doi.org/10.1093/mnras/stac3306
Advance Access publication 2022 November 12

Is the star-formation rate in $z \sim 6$ quasars overestimated?

Fabio Di Mascia,[1]★ Stefano Carniani,[1] Simona Gallerani,[1] Fabio Vito,[2] Andrea Pallottini,[1] Andrea Ferrara[1] and Milena Valentini[3,4,5]

[1]*Scuola Normale Superiore, Piazza dei Cavalieri 7, I-56126 Pisa, Italy*
[2]*INAF - Osservatorio di Astrofisica e Scienza dello Spazio di Bologna, Via Gobetti 93/3, I-40129 Bologna, Italy*
[3]*Universitäts-Sternwarte, Fakultät für Physik, Ludwig-Maximilians Universität München, Scheinerstraße 1, D-81679 München, Germany*
[4]*Excellence Cluster ORIGINS, Boltzmannstrasse 2, D-85748 Garching, Germany*
[5]*INAF - Osservatorio Astronomico di Trieste, via G.B. Tiepolo 11, I-34143 Trieste, Italy*

Accepted 2022 November 7. Received 2022 October 12; in original form 2022 June 23

ABSTRACT

The large total infrared (TIR) luminosities ($L_{\rm TIR}$; $\gtrsim 10^{12}$ L$_\odot$) observed in $z \sim 6$ quasars are generally converted into high star-formation rates (SFRs; $\gtrsim 10^2$ M$_\odot$ yr^{-1}) of their host galaxies. However, these estimates rely on the assumption that dust heating is dominated by stellar radiation, neglecting the contribution from the central active galactic nucleus (AGN). We test the validity of this assumption by combining cosmological hydrodynamic simulations with radiative transfer calculations. We find that, when AGN radiation is included in the simulations, the mass (luminosity)-weighted dust temperature in the host galaxies increases from $T \approx 50$ K ($T \approx 70$ K) to $T \approx 80$ K ($T \approx 200$ K), suggesting that AGN effectively heats the bulk of dust in the host galaxy. We compute the AGN-host galaxy SFR from the synthetic spectral energy distribution by using standard SFR – $L_{\rm TIR}$ relations, and compare the results with the 'true' values in the simulations. We find that the SFR is overestimated by a factor of $\approx$3 ($\gtrsim$10) for AGN bolometric luminosities of $L_{\rm bol} \approx 10^{12}$ L$_\odot$ ($\gtrsim 10^{13}$ L$_\odot$), implying that the SFRs of $z \sim 6$ quasars can be overestimated by over an order of magnitude.

Key words: galaxies: ISM – *(galaxies:)* quasars: general – methods: numerical – radiative transfer.

1 INTRODUCTION

In the last two decades hundreds of quasars have been discovered within the first Gyr of the Universe (e.g. Yang et al. 2020; Wang et al. 2021). These objects are powered by accreting supermassive black holes (SMBHs; 10^8–10^{10} M$_\odot$, e.g. Wu et al. 2015), shining as active galactic nucleus (AGN). Observations in the local Universe reveal that black hole (BH) masses correlate with the host-galaxy properties (e.g. Magorrian et al. 1998; Ferrarese & Merritt 2000; Gebhardt et al. 2000; Marconi & Hunt 2003; Gültekin et al. 2009), suggesting a co-evolution between the galaxy and the central SMBH (e.g. Kormendy & Ho 2013; Harrison 2017), possibly mediated by a form of feedback from the AGN via energy/momentum injections on to the surrounding gas (e.g. Silk & Rees 1998; King 2003). In this picture, AGN activity might also regulate the star formation in the host galaxy (e.g. Carniani et al. 2016; Harrison et al. 2018). A connection between the two quantities is also suggested by the similar shape of the BH accretion density and star-formation rate (SFR) density across cosmic time (e.g. Aird et al. 2015).

In the latest years, ALMA and NOEMA observations have provided the opportunity to study the properties of the interstellar medium (ISM) in several $z \sim 6$ bright quasar-host galaxies via their [C II]158 μm and CO emission, as well as the underlying dust continuum (e.g. Gallerani et al. 2017; Decarli et al. 2018; Venemans et al. 2018; Carniani et al. 2019; Venemans et al. 2020; Neeleman et al. 2021). These studies revealed the presence of large molecular gas reservoirs ($M_{\rm gas} \gtrsim 10^{10}$ M$_\odot$), dust masses ($M_{\rm dust} \approx 10^7$–$10^8$ M$_\odot$), and ongoing SFRs as high as $\approx 10^2$–10^3 M$_\odot$ yr^{-1} (e.g. Decarli et al. 2018; Venemans et al. 2020) in the host galaxies.

These estimates rely on the assumption that the far-infrared (FIR) emission is mainly due to stellar light reprocessed by dust. The FIR photometry is generally fitted with a grey-body function (e.g. Carniani et al. 2019), from which the dust mass $M_{\rm dust}$ is determined, whereas the dust temperature $T_{\rm dust}$ is assumed to be in the range of 40–60 K. The total infrared (TIR) luminosity, $L_{\rm TIR}$, is then computed by integrating the grey-body function in the wavelength range 8–1000 μm, and an SFR–$L_{\rm TIR}$ calibration (e.g. Kennicutt & Evans 2012) is used to infer the SFR in the host galaxy. This computation is very sensitive to the value of $T_{\rm dust}$, which is often set a priori because in most cases only one or a few FIR photometric data points are available (e.g. Venemans et al. 2020).

Recently, Walter et al. (2022) obtained high-angular resolution measurements of the [C II] emission and underlying dust continuum in the $z = 6.9$ quasar J2348–3054. From the fit of the spectral energy distribution (SED) they derived $T_{\rm dust} = 84.9^{+8.9}_{-10.5}$ K, and then inferred an SFR of 4700 M$_\odot$ yr^{-1}. This estimate is a factor of $\approx$10 higher than the one suggested by the [C II]–SFR relation in Herrera-Camus et al. (2018). They also found $T_{\rm dust} \geq 134$ K in the innermost region ($\approx$110 pc), implying an extreme SFR density of 10^4 M$_\odot$ yr^{-1} pc^{-2}, which is only marginally consistent with the Eddington limit for star formation (Thompson, Quataert & Murray 2005). The authors argued that this result might also be explained by a contribution from the central AGN to the dust heating in the innermost $\approx$100 pc.

★ E-mail: fabio.dimascia@sns.it

Numerical simulations constitute a complementary tool to investigate the dust properties in the ISM of galaxies, thanks to the possibility to support them with radiative transfer (RT) calculations (e.g. Behrens et al. 2018). Recently, McKinney et al. (2021) simulated a post-merger dust-enshrouded AGN, representative of submillimeter galaxies at $z \sim 2$–3. They find that AGN can dominate the dust heating on kpc scales, boosting the IR emission at $\lambda \gtrsim 100$ μm (typically associated with dust-reprocessed stellar light) by up to a factor of 4. As a consequence, standard FIR-based calibrations would overestimate the SFRs by a comparable factor. This finding is also supported by empirical works suggesting that the AGN contribution to the IR emission increases as a function of AGN power in $z \lesssim 2.5$ sources, questioning the extreme SFRs ($\gtrsim 1000$ $M_\odot$ yr^{-1}) inferred for the IR-brightest sources (Symeonidis & Page 2021; Symeonidis et al. 2022).

In this work, we test the goodness of the assumption that dust heating is dominated by stellar radiation in high-z quasar hosts exploiting numerical simulations. In Di Mascia et al. (2021, hereafter DM21), we studied the AGN contribution to the dust heating in $z \sim 6$ galaxies by post-processing the cosmological hydrodynamical simulations by Barai et al. (2018, hereafter B18), with the RT code SKIRT (Baes & Camps 2015; Camps et al. 2016). We found that in normal star-forming galaxies the dust temperature distribution is consistent with typical values adopted (40–50 K) in the SED fitting of $z > 5$ sources. However, in runs including AGN radiation the dust temperature increases to $T_{\rm dust} > 100$ K in the regions closest (≈200 pc) to the AGN, consistent with the finding by Walter et al. (2022). We expand our previous work by analysing the synthetic SEDs predicted by our simulations to investigate whether the SFR inferred from the IR emission is overestimated when the AGN contribution is not accounted for.

2 NUMERICAL METHODS

The numerical model adopted in this work is similar to DM21 and we briefly summarize it below.

2.1 Hydrodynamical simulations

We adopt the suites of cosmological hydrodynamic simulations studied in B18 and in Valentini, Gallerani & Ferrara (2021, hereafter V21). These simulations make use of a modified version of the smooth particle hydrodynamics N-body code GADGET-3 (Springel 2005) to follow the evolution of a $\sim 10^{12}$-$M_\odot$ dark matter (DM) halo in a zoom-in fashion from $z = 100$ to $z = 6$. A flat Lambda cold dark matter cosmology is assumed, with: $\Omega_{\rm M,\,0} = 0.3089$, $\Omega_{\Lambda,\,0} = 0.6911$, $\Omega_{\rm B,\,0} = 0.0486$, and $H_0 = 67.74$ km s^{-1} Mpc^{-1} (Planck Collaboration XIII 2016). The two suites differ for the particle resolution and subgrid physics implemented, as follows.

2.1.1 B18 simulations

In B18, a DM halo of $M_{\rm h} = 4.4 \times 10^{12}$ $M_\odot$ at $z = 6$ (virial radius $R_{200} = 73$ pkpc)[1] is chosen inside a comoving volume of (500 cMpc)^3 for re-simulation in a zoom-in region of (5.21 cMpc)^3. The highest resolution DM and gas particles in the zoom-in region have a mass of $m_{\rm DM} = 7.54 \times 10^6$ $M_\odot$ and $m_{\rm gas} = 1.41 \times 10^6$ $M_\odot$, respectively. Gravitational forces are softened on a scale of $\epsilon = 1\,h^{-1}$ ckpc, which corresponds to ≈210 pc at $z = 6$. The physics of the ISM is described by the multiphase model of Springel & Hernquist (2003), assuming a density threshold of $n_{\rm SF} = 0.13$ cm^{-3} for star formation and a Chabrier (2003) initial mass function in the mass range of 0.1–100 $M_\odot$. The code accounts for radiative heating and cooling, for stellar winds, supernova feedback, and metal enrichment. Stellar evolution and chemical enrichment are computed following Tornatore et al. (2007).

BHs are included in the simulation by placing a $M_{\rm BH} = 10^5$-h^{-1} $M_\odot$ BH seed at the centre of an $M_{\rm h} = 10^9$-h^{-1} $M_\odot$ DM halo, if it does not host a BH already. BHs can grow either by gas accretion or via mergers with other BHs. The former process is modelled via the Bondi–Hoyle–Littleton scheme (Hoyle & Lyttleton 1939; Bondi & Hoyle 1944; Bondi 1952), and the accretion rate is capped at the Eddington rate $\dot{M}_{\rm Edd}$. A fraction of the accreted rest-mass energy is radiated away with a bolometric luminosity:

$$L_{\rm bol} = \epsilon_{\rm r} \dot{M}_{\rm BH} c^2, \tag{1}$$

where c is the speed of light and $\epsilon_{\rm r} = 0.1$ is the radiative efficiency. AGN feedback from the accreting BHs is modelled by distributing a fraction $\epsilon_{\rm f} = 0.05$ of the energy irradiated by the BHs on to the surrounding gas in kinetic form. In this work, we consider the runs *AGNsphere* and *AGNcone* from B18, in which AGN feedback is distributed in a spherical symmetry and in a bi-cone with an half-opening angle of 45°, respectively.

2.1.2 V21 simulations

In V21, a DM halo of $M_{\rm h} = 1.12 \times 10^{12}$ $M_\odot$ is chosen for the zoom-in simulation inside a comoving volume of (148 cMpc)^3. A zoom-in region of size (5.25 cMpc)^3 is chosen for re-simulation, with the highest resolution particles of the zoom-in simulation having a mass of $m_{\rm DM} = 1.55 \times 10^6$ $M_\odot$ and $m_{\rm gas} = 2.89 \times 10^5$ $M_\odot$, respectively. The gravitational softening lengths employed are $\epsilon_{\rm DM} = 0.72$ ckpc and $\epsilon_{\rm bar} = 0.41$ ckpc for DM and baryon particles, respectively, the latter corresponding to ≈60 pc at $z = 6$, i.e. a factor of ≈3 lower than in B18. Instead of the multiphase model by Springel & Hernquist (2003), the ISM is described by means of the MUlti Phase Particle Integrator subresolution model (e.g. Murante et al. 2010; Valentini et al. 2020). It features metal cooling, thermal and kinetic stellar feedback, the presence of a ultraviolet (UV) background, and a model for chemical evolution, following Tornatore et al. (2007). In particular, star formation is implemented with an H_2-based prescription instead of a density-based criterion, as in B18.

A fraction of the accreted rest-mass energy is radiated away from the BHs according to equation (1), assuming a radiative efficiency of $\epsilon_{\rm r} = 0.03$. A fraction $\epsilon_{\rm f} = 10^{-4}$ of the radiated luminosity $L_{\rm bol}$ is thermally coupled to the gas surrounding the BHs, and it is isotropically distributed into the gas. BHs with $M_{\rm BH} = 10^5$ h^{-1} $M_\odot$ are seeded in a 10^9-h^{-1} $M_\odot$ BH-less DM halo, and they grow by accretion and mergers. In this work, we make use of the fiducial run of the suite by V21, which we will refer to as *AGNthermal*.

2.2 Radiative transfer

For each snapshot of the hydrodynamical simulations we identify all the AGNs with $L_{\rm bol} > 10^{10}$ $L_\odot$ as per equation (1). We choose for the RT post-processing a number of snapshots sufficient to well sample the AGN luminosity range between 10^{10} and 10^{14} $L_\odot$. We select for each RT simulation a cubic region of 60-kpc size (∼50 per cent of the

[1]Throughout this paper ckpc refers to *comoving* kpc and pkpc to *physical* distances in kpc. When not explicitly stated, we are referring to physical distances.

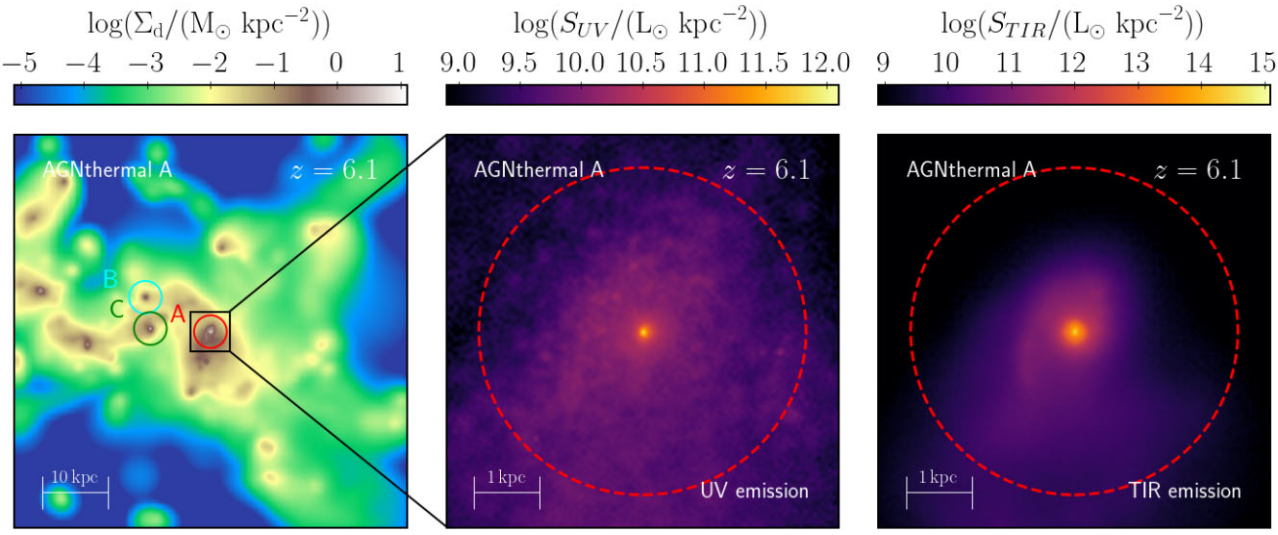

Figure 1. Maps of relevant properties relative to a representative snapshot, the $z = 6.1$ one of the run *AGNthermal*. Left-hand panel: Surface density distribution of the dust component within the computational box of 60-kpc size. The coloured circles indicate the 2.5-kpc region around each quasar host with $L_{\rm bol} > 10^{10}$ L$_\odot$, which we use to compute the dust temperature probability distribution function (PDF) in Section 3.1 and the synthetic SEDs in Section 3.2. Middle panel: UV emission predicted by our RT calculations around source A in a smaller region of 6-kpc size. The radius of 2.5 kpc is shown with a dashed red line. Right-hand panel: Same as the middle panel, but for the TIR emission.

virial radius), centred on the centre of mass of the most massive halo. We choose snapshots from different simulations in order to make our results not biased by the subgrid physics and AGN feedback prescription implemented.[2] By choosing multiple snapshots for each run, we aim to make our results more general and not depending on the specific gas/stellar morphology and AGN/star-formation activity of a single snapshot. The selected snapshots are post-processed with SKIRT[3] (Baes & Camps 2015; Camps et al. 2016). For the RT set-up, a dust component and the radiation sources need to be specified.

Given that the processes related to the dust production and destruction are not explicitly followed in the hydrodynamic simulations adopted in this work, the dust distribution is assumed to track the one of the metals. We assume a linear scaling (e.g. Draine et al. 2007) parametrized by the dust-to-metal ratio $f_{\rm d} = M_{\rm d}/M_{\rm Z}$, where $M_{\rm d}$ is the dust mass and $M_{\rm Z}$ is the total mass of all the metals in each gas particle. This parameter acts as a normalization factor for the overall dust content. In order to make our results less dependent on the specific choice of this parameter, we adopt two values for $f_{\rm d}$: a Milky Way (MW)-like value, $f_{\rm d} = 0.3$, and a lower value, $f_d = 0.08$, found to reproduce the observed SED of a $z \sim 8$ galaxy (Behrens et al. 2018). We adopt dust optical properties of the Small Magellanic Cloud (SMC; Weingartner & Draine 2001). We assume gas particles hotter than 10^6 K to be dust-free because of thermal sputtering (e.g. Draine & Salpeter 1979).

Dust is distributed in the computational domain in an octree grid, whose maximum number of levels of refinement for high-dust density regions is chosen according to the spatial resolution of the hydrodynamic simulations. For the runs from B18, we adopt eight levels of refinement, achieving a spatial resolution of ≈230 pc in the most refined cells, comparable with the softening length in the hydrodynamic simulation (≈210 pc at $z = 6$); for the runs from V21, we adopt 10 levels of refinement, with the highest resolved cells having a size of ≈59 pc, consistent with the softening length (≈87 pc at $z = 6$). For illustration purposes, in Fig. 1 we show the dust surface density distribution for the snapshot at $z = 6.1$ of the run *AGNthermal*, which we consider as a representative case. Within the simulated computational box, three quasar-host galaxies with $L_{\rm bol} > 10^{10}$ L$_\odot$ are present, and are labelled in the figure.

We make use of the stellar synthesis models by Bruzual & Charlot (2003) to implement the stellar radiation, according to the mass, age, and metallicity of each stellar particle. For the BHs, we use the composite power-law AGN SED we introduced in DM21, which is derived on the basis of several observational and theoretical works (Shakura & Sunyaev 1973; Fiore et al. 1994; Richards et al. 2003; Sazonov, Ostriker & Sunyaev 2004; Piconcelli et al. 2005; Gallerani et al. 2010; Lusso et al. 2015; Shen et al. 2020). The AGN SED reads

$$L_\lambda = c_i \left(\frac{\lambda}{\mu\rm m}\right)^{\alpha_i} \left(\frac{L_{\rm bol}}{\rm L_\odot}\right) \rm L_\odot\ \mu m^{-1}, \quad (2)$$

where i labels the bands in which we decompose the spectra and the coefficients c_i are determined by imposing the continuity of the function based on the slopes α_i, as detailed in table 2 in DM21. In particular, we make use of the *fiducial* AGN SED, characterized by an UV spectral slope $\alpha_{\rm UV} = -1.5$. The SED is then normalized according to the bolometric luminosity of the AGN (see equation 1). The radiation field is sampled by using a grid composed of 200 logarithmically spaced bins, covering the *rest-frame* wavelength range $[0.1-10^3]$ μm, with 10^6 photon packets launched from each source per wavelength bin.

In order to isolate the contribution of the AGN to dust heating, we perform each RT run with and without AGN radiation: We refer to the first group of simulations as *AGN on*, and to the second as *AGN off*. The runs *AGN off* and *AGN on* share the same dust/stellar content and distribution: They differ from each other solely in the AGN contribution to the radiation field.

As an illustrative case, we show in the middle and right-hand panels of Fig. 1 the UV (0.1−0.3 μm) and TIR (8−1000 μm) emission in a zoomed region around source A.

[2]Different feedback prescriptions can significantly affect the gas/metals distribution and the star formation, as already shown in the original work by B18 and V21, and also in DM21 (see their fig. 1) and Vito et al. (2022).
[3]Version 8, http://www.skirt.ugent.be.

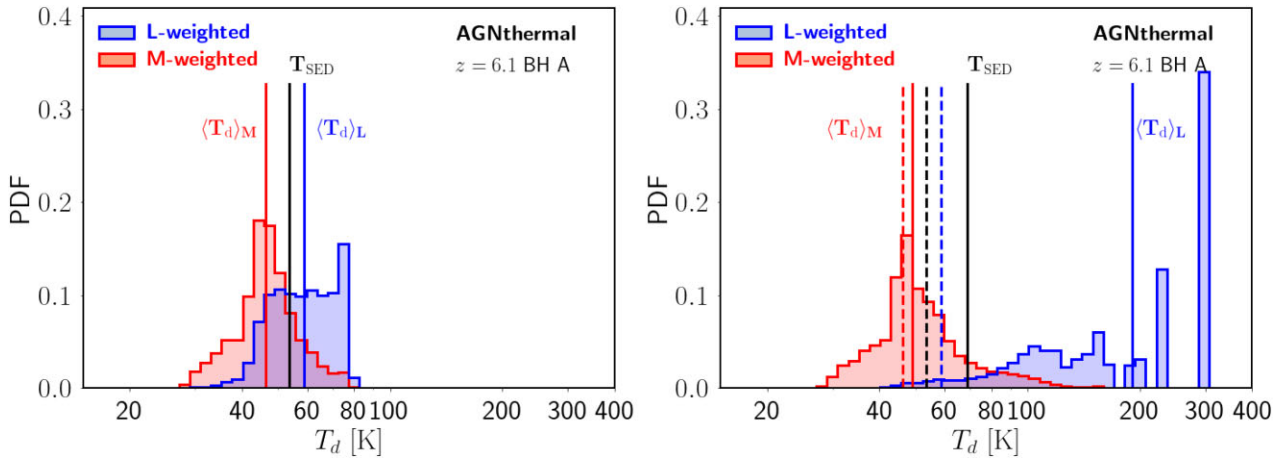

Figure 2. Left-hand panel: PDF of the mass-weighted (red) and luminosity-weighted (blue) dust temperature (see Section 3.1) of the computational cells within 2.5 kpc from a representative AGN (i.e. source A in Fig. 1) in the *AGN off* case. The red and blue solid lines mark the median values of the mass-weighted and luminosity-weighted PDFs, $T_{d,M}$ and $T_{d,L}$, respectively. The black solid line indicates the value of T_{SED} derived from the SED fitting (see Section 3.2). Right-hand panel: Same as the left-hand panel, but for the *AGN on* case. For comparison, we also show in this panel the values of $T_{d,M}$, $T_{d,L}$, and T_{SED} for the *AGN off* case with dashed lines, adopting the same colour legend as in the left-hand panel.

3 AGN CONTRIBUTION TO DUST HEATING

We now investigate the contribution of the AGN radiation to the dust heating, by comparing the dust temperature distribution of the *AGN on* and *AGN off* runs. We first analyse the actual dust temperature in the host galaxies in Section 3.1; then we discuss in Section 3.2 the dust temperature that would be inferred for our quasar hosts by treating our synthetic SEDs as mock observations.

3.1 Physical dust temperature

For each RT run, we select the region within 2.5 kpc around each AGN, which encloses the AGN host. This size is comparable to the galaxy sizes in the simulations and to the dust continuum size of the majority of the quasar hosts observed at $z \sim 6$ (e.g. Venemans et al. 2020). The dust masses in the AGN hosts are in the range of 3.1×10^6–2.0×10^8 $M_\odot$, whereas the AGN bolometric luminosities are $L_{bol} = 10^{10}$–10^{14} $L_\odot$. We compute the PDF of the dust temperatures in this region for the *AGN off* and *AGN on* runs as done in DM21. For each AGN, we consider the cells in the dust grid within 2.5 kpc from the BH, and we compute the mass-weighted dust temperature PDF $\langle T_d \rangle_M$ by weighting the dust temperature in each cell $T_{d,i}$ with its dust mass $M_{d,i}$. We also compute the luminosity-weighted dust temperature PDF $\langle T_d \rangle_L$, assuming that each cell emits as a grey-body $L_{TIR,i} \propto M_{d,i} T_{d,i}^{4+\beta_d}$, where β_d is the dust emissivity index (see Section 3.2), which for this calculation is set to $\beta_d = 2$.[4] Finally, we compute the median values of the PDFs within the 2.5-kpc regions, $\langle T_d \rangle_M$ and $\langle T_d \rangle_L$, and we indicate these medians with $T_{d,M}$ and $T_{d,L}$, respectively. The latter is expected to be dominated by the hottest regions in the AGN proximity, whereas the former should be more representative of the bulk of the dust in the ISM. As an example, in Fig. 2, we compare the PDFs in the *AGN off* and *AGN on* cases derived for the representative quasar host also used in Fig. 1. The presence of AGN radiation shifts the dust temperature distribution towards higher values. This effect is significant for the luminosity-weighted distribution; however, it is also noticeable in the mass-weighted one.

In order to analyse in a more systematic way the effect of the AGN radiation on the dust temperature distributions, we compare the median values of the weighted PDFs for all of the considered *AGN off* and *AGN on* cases in Fig. 3. We find that although $T_{d,L} < 70$ K in the *AGN off* cases, in agreement with the values usually assumed in observations to derive M_d and SFR, it increases up to $T_{d,L} \approx 250$ K in the *AGN on* runs, when AGN radiation is accounted for, showing a strong trend with AGN luminosity. This result is consistent with what found in Di Mascia et al. (2021): AGN radiation can effectively heat dust in the ISM on ≈200-pc scales from the AGN.

A similar trend is also found for the mass-weighted dust temperature, even if less pronounced. In fact, while $T_{d,M} \lesssim 50$ K in the *AGN off* runs, it increases up to $T_{d,M} \approx 80$ K in the *AGN on* runs. This result has important consequences: It implies that AGN can heat the bulk of the ISM dust in their host galaxies, not only in their proximity. The behaviour of $T_{d,M}$ is also found to correlate with the AGN luminosity. In both the mass-weighted and luminosity-weighted distributions, the median dust temperatures in *AGN on* runs start to deviate (see Fig. 3) from the *AGN off* values already at $L_{bol} \approx 10^{12}$ $L_\odot$ for most of the AGN hosts. For $L_{bol} \gtrsim 10^{13}$ $L_\odot$, $T_{d,M}$ increases by 20−50 per cent. This is a significant effect: Since the TIR luminosity scales approximately as $L_{TIR} \propto T_{dust}^{4+\beta}$ (where $\beta \approx 2$ is the dust emissivity index, see Section 3.2), a 50 per cent boost from the AGN radiation results in a 10-fold increase of the total IR luminosity. Given that most of the quasars detected at $z > 6$ have bolometric luminosities larger than 10^{13} $L_\odot$ (e.g. Yang et al. 2021), our calculations suggest that AGNs dominate the dust heating in the majority of these sources.

3.2 Dust temperature inferred from the SED

We derive the synthetic SED of each AGN host by considering the radiation emitted within 2.5 kpc from the position of the BHs, consistently with the analysis in Section 3. The SED of a representative quasar host is shown in Fig. 4. We then treat the SEDs as mock observations and we perform an SED fitting of the FIR emission.

[4]We verified that varying $1.5 < \beta_d < 2.5$ does not change significantly our results.

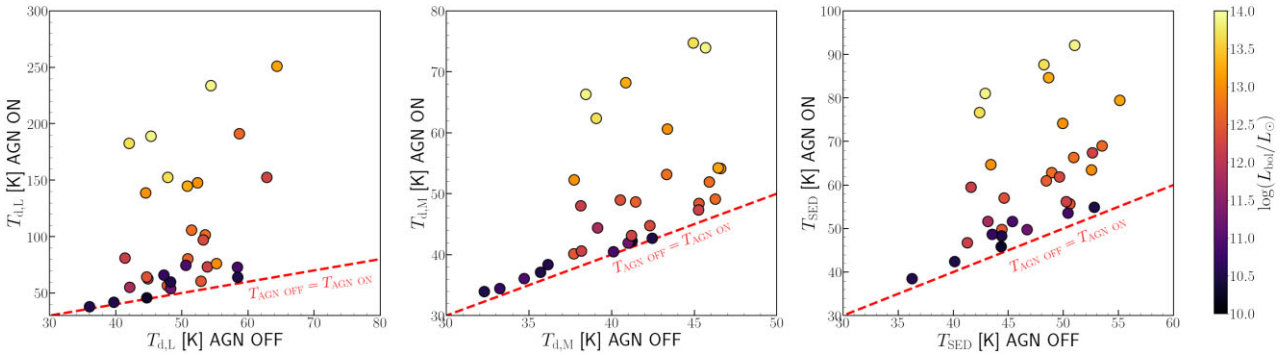

Figure 3. Comparison of different proxies of dust temperature distribution between the *AGN off* and *AGN on* cases for all the considered AGN and snapshots. Left-hand panel: Median of the luminosity-weighted dust temperature $T_{d,L}$. Middle panel: Median of the mass-weighted dust temperature $T_{d,M}$. Right-hand panel: SED-derived dust temperature T_{SED} (see Section 3.2). Each run is colour-coded according to the AGN bolometric luminosity. The dashed red lines mark the locus where temperatures in the *AGN on* and *AGN off* cases are equal.

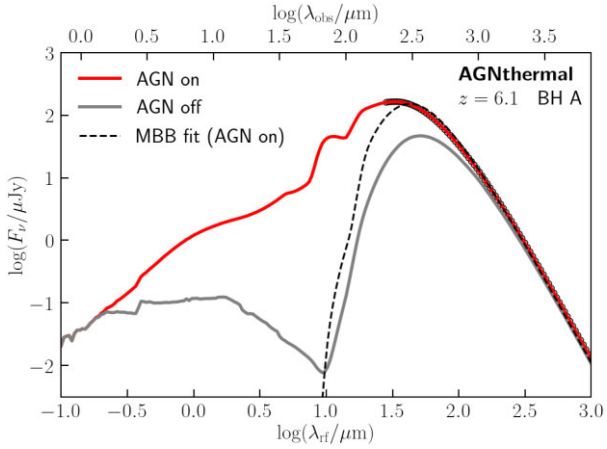

Figure 4. SED emitted from the 2.5 kpc-sized area selected around a representative quasar host (source A in Fig. 1). The solid red line shows the flux for the *AGN on* RT run and the grey solid line the *AGN off* case. The black dashed line indicate the SED fit of the rest-frame FIR part of the SED performed according to the modified blackbody function (equation 3). The black circles indicate the points of the SED used for the fit.

The dust emission in the optically thin limit can be expressed as (e.g. Carniani et al. 2019)

$$S^{obs}_{\nu_{obs}} = \frac{1+z}{d_L^2}\, M_{dust}\, \kappa_\nu\, B_\nu(T_{SED}), \tag{3}$$

where $S^{obs}_{\nu_{obs}}$ represents the observed flux at the observed frequency ν_{obs} and $B_\nu(T_{SED})$ is the blackbody emission at the dust temperature T_{SED}. We underline that T_{SED} should not be interpreted as a 'true' dust temperature of the dust component in the galaxy, which has instead a complex multitemperature distribution (see appendix A in Sommovigo et al. 2021 for an in-depth discussion). The dust opacity κ_ν is usually expressed as a power law $\kappa_0 \left(\frac{\lambda_0}{\lambda}\right)^\beta$, with the parameters κ_0, λ_0 and the dust emissivity index β derived from theoretical models (e.g. Weingartner & Draine 2001; Bianchi & Schneider 2007) or from observations (e.g. Beelen et al. 2006; Valiante et al. 2011). We adopt the dust opacity κ_ν appropriate for the SMC dust model from Weingartner & Draine (2001), the same used in the RT simulations. This leaves the dust mass M_{dust} and the dust temperature T_{dust} as the only free parameters. In most observations of $z \sim 6$ quasar hosts, only one or a few data points in the rest-frame FIR are available (e.g. Venemans et al. 2020), without probing the SED peak; therefore, the estimate of T_{SED} is very uncertain, with few notable exceptions (e.g. Pensabene et al. 2021). In order to avoid this problem, we consider the FIR portion of our synthetic SEDs at $\lambda_{obs} > 200$ μm (corresponding to more than 70 bins of the wavelength grid), which is the wavelength range typically probed by $z \sim 6$ quasar observations, and we assign a 10 per cent error to the flux at each wavelength, in order to mimic the typical experimental uncertainties (e.g. Venemans et al. 2020).

In Fig. 2, we mark the value of T_{SED} for the representative quasar host shown in Fig. 1. T_{SED} has an intermediate value between $\langle T_d \rangle_M$ and $\langle T_d \rangle_L$. It also tends to be more similar to the median of the mass-weighted distribution rather than to the luminosity-weighted one in the *AGN on* cases. In the right-most panel of Fig. 3, we show how the measured values of T_{SED} change when including AGN radiation for all the simulated quasar hosts. We find a significant increase of the estimated T_{SED} when AGN radiation is included, from $T_{SED} \lesssim 60$ K in the *AGN off* to $T_{SED} \approx 90$ K in the *AGN on* runs. In particular, we notice that all the simulated galaxies with $T_{SED} \gtrsim 60$ K are among *AGN on* runs, suggesting that galaxies with $T_{SED} \gtrsim 60$ K are likely AGN-powered. A trend with the AGN bolometric luminosity is also present, with the most luminous AGN showing the largest increase of T_{SED}. This result is consistent with the behaviour of the mass-weighted and luminosity-weighted PDFs shown in Fig. 3, as T_{SED} partly reflects the actual dust temperature distribution in the AGN host. Therefore, the correlation found in Fig. 3 is a direct consequence of the AGN heating of the ISM dust in the simulated galaxies, as seen in the behaviour of $T_{d,L}$ and $T_{d,M}$ (left-hand and middle panels of Fig. 3).

In Fig. 5, we show the ratio of the values obtained for these three indicators of the dust temperature distribution. As expected, all the ratios increase with L_{bol}, with the shallowest (steepest) rise for the mass-weighted (luminosity-weighted) median; T_{SED} is intermediate between the two. In particular, we note that for the brightest AGN, $L_{bol} \gtrsim 10^{13}\ L_\odot$, the SED-derived dust temperature T_{SED} increases by a factor of almost 2, similarly to the median of the mass-weighted $T_{d,M}$.

4 SFR ESTIMATE FROM THE FIR

The analysis in Section 3 shows that in the simulated $z \sim 6$–7 galaxies, AGN radiation can contribute significantly to dust heating, affecting the temperature of the bulk of the dust in the ISM. Given that the SFR estimates in high-z quasar hosts are based on the assumption that stellar radiation is the only source of dust heating in the host galaxy, we investigate the impact of the AGN contribution

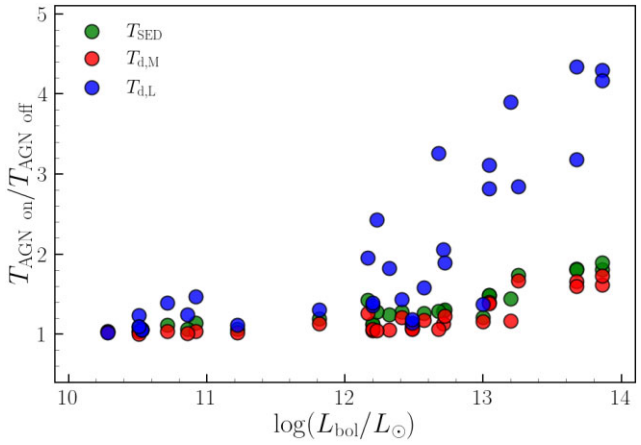

Figure 5. Ratio of the *AGN on* to *AGN off* runs for the median of the luminosity-weighted temperature $T_{\rm d,\,L}$ (blue circles), the median of the mass-weighted temperature $T_{\rm d,\,M}$ (red circles), and $T_{\rm SED}$ (green circles) as a function of the bolometric luminosity of the AGN.

on the inferred SFR values. We now take advantage of our RT simulations by using our synthetic SEDs as mock observations as in Section 3.2. Then, we estimate the SFR in the host galaxy from the FIR luminosity, assuming that dust is heated only by stars. Finally, we compare the inferred SFR with the actual SFR in the quasar hosts, which is known from the hydrodynamic simulations.

For each simulated AGN host, we estimate the SFR from our synthetic SEDs as follows. We compute the total IR luminosity $L_{\rm TIR}$ by integrating equation (3) over the wavelength range 8−1000 μm. Then, we make use of the $\rm SFR_{FIR}$–$L_{\rm TIR}$ calibration in Kennicutt & Evans (2012), based on Murphy et al. (2011). This relation provides an estimate of the *obscured* SFR, i.e. the stellar radiation that is absorbed by dust, *assuming that dust heating is purely due to stars*. We perform this computation both for the *AGN off* and the *AGN on* runs, in order to quantify the AGN contribution to the SFR estimate.

For *AGN off* runs we also include the *unobscured* SFR, by adopting the $\rm SFR_{UV}$–$L_{\rm FUV}$ calibration from Kennicutt & Evans (2012).[5] The contribution of $\rm SFR_{UV}$ is not accounted for in the *AGN on* runs, consistently with observational works, since the UV emission is expected to be dominated by the quasar. We note that accounting also for $\rm SFR_{UV}$ would increase the discrepancies between the inferred SFRs in the *AGN on* and *AGN off* cases, thus reinforcing our conclusions.

We compare the SFR inferred from the SED as described above with the actual SFR in the AGN hosts, which is known from the hydrodynamical simulations. The SFR is computed in the region within 2.5 kpc from the position of each BH in order to be consistent with the synthetic SED. We consider the SFR averaged over the past 100 Myr, which we found to provide the best agreement with the UV calibration in the *AGN off* runs. Fig. 6 presents the ratio of the SED-based SFR to the true SFR as a function of the AGN bolometric luminosity. For the runs without AGN radiation the SFR estimated from the SED fitting is overall in agreement with the actual SFR in the AGN hosts (see black histogram in the right-hand panel of Fig. 6). This consistency check demonstrates that our procedure

[5]We use the results from Madau & Dickinson (2014) – see their Fig. 4 – to correct the conversion factor, in order to take into account the different initial mass function adopted in the simulations (Chabrier 2003) with respect to the one used in the Kennicutt & Evans (2012) calibration (Kroupa & Weidner 2003).

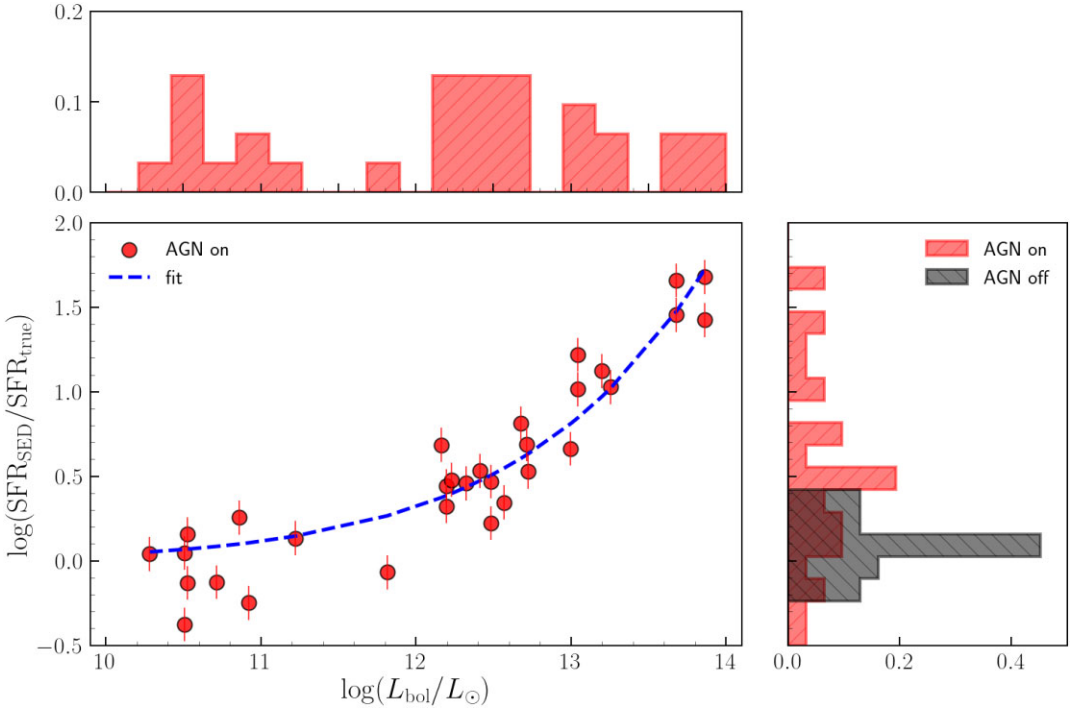

Figure 6. Ratio of the total SFR (estimated via FIR SED fitting, as explained in Section 4) to the true SFR in the AGN hosts as a function of the luminosity of the AGN. The blue dashed line indicates the exponential fit as in equation (4). The upper inset shows the distribution of AGN luminosities. The inset on the right hand shows the distribution of the $\rm SFR_{SED}$ to $\rm SFR_{true}$ ratio for the *AGN on* and *AGN off* runs in red and black histograms, respectively. We note that the distribution of the SFR estimates of the *AGN off* runs is consistent with the actual SFR.

correctly recovers the SFR in the host galaxy if dust heating due to AGN radiation is negligible.

In the *AGN on* runs, the SFR inferred from the SED tends to overestimate the actual SFR, with a discrepancy that becomes significant (a factor ≈3) at bolometric luminosities $L_{\rm bol} = 10^{12}$ L$_\odot$, and approximately an order of magnitude of discrepancy for most of the runs at $L_{\rm bol} \gtrsim 10^{13}$ L$_\odot$. This behaviour is consistent with our findings in Section 3, in particular with the trend of $T_{\rm SED}$ between *AGN on* and *AGN off* runs as a function of AGN luminosity. As discussed in Section 3, an increase by a factor of ≈2 in the dust temperature results in ≈10-fold increase in the TIR luminosity. Given that the IR luminosity is assumed to come from dust-reprocessed stellar light only, also the inferred SFR increases by the same factors.

We fit the relation $\log(\mathrm{SFR_{SED}}/\mathrm{SFR_{true}})$ versus $\log(L_{\rm bol}/\mathrm{L_\odot})$ with a power-law expression, finding

$$\log\left(\frac{\mathrm{SFR_{SED}}}{\mathrm{SFR_{true}}}\right) = 7.68 \times 10^{-14}\left[\log\left(\frac{L_{\rm bol}}{\mathrm{L_\odot}}\right)\right]^{11.7}. \quad (4)$$

This relation quantifies the overestimate of the SFR in AGN hosts at $z \gtrsim 6$, as a function of their bolometric luminosity. It can be applied to correct the SFR in quasar hosts with observed luminosity in the range $10^{10} \lesssim L_{\rm bol}/\mathrm{L_\odot} \lesssim 10^{14}$, and a well-constrained $T_{\rm SED}$ from the SED fitting. We assign a 0.15-dex uncertainty to this expression based on the scatter between the same run performed with different values of the dust-to-metal ratio.

As a practical case, we apply this correction to the quasar J2348−3054, recently studied in Walter et al. (2022). Instead of SFR ≈ 4700 M$_\odot$ yr^{-1}, we find an SFR ≈ 370 M$_\odot$ yr^{-1}, in broad agreement with the [C II]-inferred SFR ≈ 530 M$_\odot$ yr^{-1} from the relation by Herrera-Camus et al. (2018).

5 CONCLUSIONS

We investigated whether stellar radiation can be considered the main source of dust heating in $z \sim 6$ quasar hosts, and the reliability of the SFR inferred from the TIR (8−1000 μm) emission in these galaxies. We combined cosmological hydrodynamic simulations with RT calculations, and simulated each galaxy with and without AGN radiation, in order to isolate the AGN contribution to dust heating.

We find that AGNs with $L_{\rm bol} \gtrsim 10^{13}$ L$_\odot$ effectively heat the bulk of the dust in the ISM on galaxy scales, and not only the dust on ≈100 pc from their surroundings. As a result, the actual IR emission that comes from dust-reprocessed stellar light can be significantly overestimated.

We quantify this effect by applying the SFR–$L_{\rm TIR}$ relation by Kennicutt & Evans (2012) to the synthetic SEDs of the simulated quasar hosts, and compare the results with the 'true' SFR in the hydrodynamic simulations. We find that the SFR tends to be overestimated by a factor of ≈3 (≈30) for $L_{\rm bol} \approx 10^{12}$ L$_\odot$ ($L_{\rm bol} \approx 10^{13}$ L$_\odot$, see Fig. 6). We also provide a simple relation (equation 4) that quantifies the overestimate of the SFR in terms of the AGN luminosity.

We note that our results might be sensitive to the spatial resolution of the hydrodynamic simulations adopted in this work, the assumed models for the ISM physics, and to the numerical set-up of the RT calculations. It would be valuable to repeat this analysis using simulations achieving higher spatial resolutions and a different implementation of the RT calculations.

ACKNOWLEDGEMENTS

SC is supported by European Union's HE ERC Starting Grant No. 101040227 - WINGS. SG acknowledges support from the ASI-INAF n. 2018-31-HH.0 grant and PRIN-MIUR 2017. AP and AF acknowledge support from the ERC Advanced Grant INTERSTELLAR H2020/740120 (PI: Ferrara). Any dissemination of results must indicate that it reflects only the author's view and that the Commission is not responsible for any use that may be made of the information it contains. MV is supported by the Alexander von Humboldt-Stiftung and the Carl Friedrich von Siemens Stiftung. MV also acknowledges support from the Excellence Cluster ORIGINS, which is funded by the Deutsche Forschungsgemeinschaft (DFG, German Research Foundation) under Germany's Excellence Strategy - EXC-2094 - 390783311. We acknowledge usage of the PYTHON programming language (Van Rossum & de Boer 1991; Van Rossum & Drake 2009), ASTROPY (Astropy Collaboration et al. 2013), CYTHON (Behnel et al. 2011), MATPLOTLIB (Hunter 2007), NUMPY (van der Walt, Colbert & Varoquaux 2011), PYNBODY (Pontzen et al. 2013), and SCIPY (Virtanen et al. 2020). We gratefully acknowledge computational resources of the Center for High Performance Computing (CHPC) at Scuola Normale Superiore, Pisa (Italy).

DATA AVAILABILITY

The derived data generated in this research will be shared on reasonable request to the corresponding author.

REFERENCES

Aird J., Coil A. L., Georgakakis A., Nandra K., Barro G., Pérez-González P. G., 2015, MNRAS, 451, 1892
Astropy Collaboration et al., 2013, A&A, 558, A33
Baes M., Camps P., 2015, Astron. Comput., 12, 33
Barai P., Gallerani S., Pallottini A., Ferrara A., Marconi A., Cicone C., Maiolino R., Carniani S., 2018, MNRAS, 473, 4003 (B18)
Beelen A., Cox P., Benford D. J., Dowell C. D., Kovács A., Bertoldi F., Omont A., Carilli C. L., 2006, ApJ, 642, 694
Behnel S., Bradshaw R., Citro C., Dalcin L., Seljebotn D., Smith K., 2011, Comput. Sci. Eng., 13, 31
Behrens C., Pallottini A., Ferrara A., Gallerani S., Vallini L., 2018, MNRAS, 477, 552
Bianchi S., Schneider R., 2007, MNRAS, 378, 973
Bondi H., 1952, MNRAS, 112, 195
Bondi H., Hoyle F., 1944, MNRAS, 104, 273
Bruzual G., Charlot S., 2003, MNRAS, 344, 1000
Camps P., Trayford J. W., Baes M., Theuns T., Schaller M., Schaye J., 2016, MNRAS, 462, 1057
Carniani S. et al., 2016, A&A, 591, A28
Carniani S. et al., 2019, MNRAS, 489, 3939
Chabrier G., 2003, PASP, 115, 763
Decarli R. et al., 2018, ApJ, 854, 97
Di Mascia F. et al., 2021, MNRAS, 503, 2349 (DM21)
Draine B. T., Salpeter E. E., 1979, ApJ, 231, 77
Draine B. T. et al., 2007, ApJ, 663, 866
Ferrarese L., Merritt D., 2000, ApJ, 539, L9
Fiore F., Elvis M., McDowell J. C., Siemiginowska A., Wilkes B. J., 1994, ApJ, 431, 515
Gallerani S. et al., 2010, A&A, 523, A85
Gallerani S., Fan X., Maiolino R., Pacucci F., 2017, Publ. Astron. Soc. Aust., 34, e022
Gebhardt K. et al., 2000, ApJ, 539, L13
Gültekin K. et al., 2009, ApJ, 698, 198
Harrison C. M., 2017, Nature Astron., 1, 0165

Harrison C. M., Costa T., Tadhunter C. N., Flütsch A., Kakkad D., Perna M., Vietri G., 2018, Nature Astron., 2, 198
Herrera-Camus R. et al., 2018, ApJ, 861, 95
Hoyle F., Lyttleton R. A., 1939, Proc. Camb. Phil. Soc., 35, 405
Hunter J. D., 2007, Comput. Sci. Eng., 9, 90
Kennicutt R. C., Evans N. J., 2012, ARA&A, 50, 531
King A., 2003, ApJ, 596, L27
Kormendy J., Ho L. C., 2013, ARA&A, 51, 511
Kroupa P., Weidner C., 2003, ApJ, 598, 1076
Lusso E., Worseck G., Hennawi J. F., Prochaska J. X., Vignali C., Stern J., O'Meara J. M., 2015, MNRAS, 449, 4204
McKinney J., Hayward C. C., Rosenthal L. J., Martínez-Galarza J. R., Pope A., Sajina A., Smith H. A., 2021, ApJ, 921, 55
Madau P., Dickinson M., 2014, ARA&A, 52, 415
Magorrian J. et al., 1998, AJ, 115, 2285
Marconi A., Hunt L. K., 2003, ApJ, 589, L21
Murante G., Monaco P., Giovalli M., Borgani S., Diaferio A., 2010, MNRAS, 405, 1491
Murphy E. J. et al., 2011, ApJ, 737, 67
Neeleman M. et al., 2021, ApJ, 911, 141
Pensabene A. et al., 2021, A&A, 652, A66
Piconcelli E., Jimenez-Bailón E., Guainazzi M., Schartel N., Rodríguez-Pascual P. M., Santos-Lleó M., 2005, A&A, 432, 15
Planck Collaboration XIII, 2016, A&A, 594, A13
Pontzen A., Roskar R., Stinson G. S., Woods R., Reed D. M., Coles J., Quinn T. R., 2013, pynbody: N-Body/SPH analysis for python, Astrophysics Source Code Library [record ascl:1305.002]
Richards G. T. et al., 2003, AJ, 126, 1131
Sazonov S. Y., Ostriker J. P., Sunyaev R. A., 2004, MNRAS, 347, 144
Shakura N. I., Sunyaev R. A., 1973, A&A, 500, 33
Shen X., Hopkins P. F., Faucher-Giguère C.-A., Alexander D. M., Richards G. T., Ross N. P., Hickox R. C., 2020, MNRAS, 495, 3252
Silk J., Rees M. J., 1998, A&A, 331, L1
Sommovigo L., Ferrara A., Carniani S., Zanella A., Pallottini A., Gallerani S., Vallini L., 2021, MNRAS, 503, 4878
Springel V., 2005, MNRAS, 364, 1105
Springel V., Hernquist L., 2003, MNRAS, 339, 289
Symeonidis M., Page M. J., 2021, MNRAS, 503, 3992
Symeonidis M. et al., 2022, MNRAS, 514, 4450
Thompson T. A., Quataert E., Murray N., 2005, ApJ, 630, 167
Tornatore L., Borgani S., Dolag K., Matteucci F., 2007, MNRAS, 382, 1050
Valentini M. et al., 2020, MNRAS, 491, 2779
Valentini M., Gallerani S., Ferrara A., 2021, MNRAS, 507, 1 (V21)
Valiante R., Schneider R., Salvadori S., Bianchi S., 2011, MNRAS, 416, 1916
van der Walt S., Colbert S. C., Varoquaux G., 2011, Comput. Sci. Eng., 13, 22
Van Rossum G., de Boer J., 1991, CWI Q., 4, 283
Van Rossum G., Drake F. L., 2009, Python 3 Reference Manual. CreateSpace, Scotts Valley, CA
Venemans B. P. et al., 2018, ApJ, 866, 159
Venemans B. P. et al., 2020, ApJ, 904, 130
Virtanen P. et al., 2020, Nature Methods, 17, 261
Vito F., Di Mascia F., Gallerani S., Zana T., Ferrara A., Carniani S., Gilli R., 2022, MNRAS, 514, 1672
Walter F. et al., 2022, ApJ, 927, 21
Wang F. et al., 2021, ApJ, 907, L1
Weingartner J. C., Draine B. T., 2001, ApJ, 548, 296
Wu X.-B. et al., 2015, Nature, 518, 512
Yang J. et al., 2020, ApJ, 897, L14
Yang J. et al., 2021, ApJ, 923, 262

This paper has been typeset from a TEX/LATEX file prepared by the author.